

EDA-DM: Enhanced Distribution Alignment for Post-Training Quantization of Diffusion Models

Xuwen Liu^{1,2}, Zhikai Li^{1,2}*, Junrui Xiao^{1,2}, Qingyi Gu¹*

¹Institute of Automation, Chinese Academy of Sciences

²School of Artificial Intelligence, University of Chinese Academy of Sciences

Abstract

Diffusion models have achieved great success in image generation tasks through iterative noise estimation. However, the heavy denoising process and complex neural networks hinder their low-latency applications in real-world scenarios. Quantization can effectively reduce model complexity, and post-training quantization (PTQ), which does not require fine-tuning, is highly promising for compressing and accelerating diffusion models. Unfortunately, we find that due to the highly dynamic distribution of activations in different denoising steps, existing PTQ methods for diffusion models suffer from distribution mismatch issues at both calibration sample level and reconstruction output level, which makes the performance far from satisfactory, especially in low-bit cases. In this paper, we propose Enhanced Distribution Alignment for Post-Training Quantization of Diffusion Models (EDA-DM) to address the above issues. Specifically, at the calibration sample level, we select calibration samples based on the density and variety in the latent space, thus facilitating the alignment of their distribution with the overall samples; and at the reconstruction output level, we modify the loss of block reconstruction with the losses of layers, aligning the outputs of quantized model and full-precision model at different network granularity. Extensive experiments demonstrate that EDA-DM significantly outperforms the existing PTQ methods across various models (DDIM, LDM-4, LDM-8, Stable-Diffusion) and different datasets (CIFAR-10, LSUN-Bedroom, LSUN-Church, ImageNet, MS-COCO).

Introduction

Recently, diffusion models have gradually gained prominence in image generation tasks (Li et al. 2022a; Lugmayr et al. 2022; Zhang, Rao, and Agrawala 2023; Zhang et al. 2023; Niu et al. 2020). Both considering the quality and diversity, they can compare or even outperform the SoTA GAN models (Phung, Dao, and Tran 2023; Ozbey et al. 2023). Furthermore, the flexible extensions of diffusion models achieve great performance in many downstream tasks, such as super-resolution (Li et al. 2022a), inpainting (Lugmayr et al. 2022), text-to-image translation (Zhang, Rao, and Agrawala 2023), style transfer (Zhang et al. 2023), and graph generation (Niu et al. 2020).

Nevertheless, the heavy denoising process and complex neural networks hinder their low-latency applications in

real-world scenarios. To accelerate diffusion models, previous works (Nichol and Dhariwal 2021; Song, Meng, and Ermon 2020; Zhang, Tao, and Chen 2022; Lu et al. 2022; Watson et al. 2022) have focused on finding shorter and more efficient generation trajectories, thus reducing the number of steps in the denoising process. Unfortunately, the complex network they ignored is also an important factor that consumes high memory and slows down the model at each denoising step. For instance, even in the high-performance A6000, Stable-Diffusion (Rombach et al. 2022) still takes over a second to perform one denoising step with 16GB GPU memory. Compression techniques not only accelerate network, but also reduce the model memory footprint, which are extremely beneficial for generalizing diffusion models in low-latency applications.

Quantization is one of the most popular model compression methods, which includes two main approaches: quantization-aware training (QAT) and post-training quantization (PTQ). While QAT can maintain performance by fine-tuning the whole models, it requires a significant amount of training data and expensive resources. For instance, TDQ (So et al. 2024) retrains DDIM on CIFAR-10 using a 50K original dataset with 200K iterations. EfficientDM (He et al. 2023a) utilizes an additional LoRA module to fine-tune DDIM on CIFAR-10 with 12.8K iterations and 819.2K samples. On the other hand, PTQ exhibits efficiency in terms of both data and time usage, which is more desired for compressing diffusion models.

PTQ generally follows a simple pipeline: obtaining calibration samples and then reconstructing the output. However, previous PTQ methods designed for a single time step network fail in diffusion models because the activations in different denoising steps lead to a distribution mismatch at two levels: **1) At calibration sample level**, since the diffusion models have an iterative denoising process, the temporal activations result in input samples changed with time steps, making it difficult to align calibration samples with the overall sample distribution. (Shang et al. 2023), (Li et al. 2023b), and (Wang et al. 2023) propose specific calibration samples to address this issue. However, these methods are suboptimal or introduce computational overhead. **2) At reconstruction output level**, the activations in diffusion models have a wide range, which increases the difficulty of quantization. Using the previous reconstruction methods re-

*Corresponding author: {lizhikai2020, qingyi.gu}@ia.ac.cn.

sults in the outputs mismatch between the quantized model and the full-precision model. Specifically, block-wise reconstruction (Li et al. 2021) over-enhances the dependence within the block layers, while layer-wise reconstruction (Xu et al. 2021) ignores the connections across layers.

To address the above issues, we propose a novel PTQ method for diffusion models, Enhanced Distribution Alignment for Post-Training Quantization of Diffusion Models (EDA-DM). At the calibration sample level, we extract information from the feature maps in the latent space for guiding the selection of calibration samples. Based on the density and variety of feature maps, the Temporal Distribution Alignment Calibration (TDAC) we selected effectively aligns the distribution of the calibration samples with that of the overall samples. At the reconstruction output level, we propose Fine-grained Block Reconstruction (FBR), which modifies the loss of a block by incorporating the losses of layers within the block. This approach mitigates over-dependence within the block and enhances the connections between layers, aligning the outputs of quantized models and full-precision models at different network granularity. To the best of our knowledge, existing PTQ methods for diffusion models ignore the effect of reconstruction, while this is the first work to analyze and improve the reconstruction method based on the properties of diffusion models. Overall, our contributions are summarized as follows:

- Through thorough analysis, we identify two levels of mismatch in diffusion models, including the calibration sample level and the reconstruction output level, which result in the low performance of PTQ.
- Based on the above insight, we propose EDA-DM, an efficient PTQ method for compressing and accelerating diffusion models. Specifically, we propose TDAC to address the calibration sample level mismatch, and propose FBR to eliminate the reconstruction output level mismatch.
- Extensive results show that EDA-DM significantly outperforms the existing PTQ methods for diffusion models, especially in low-bit cases. Additionally, EDA-DM demonstrates robustness across various factors such as model scale, resolution, and guidance conditions.

Related work

Efficient Diffusion Models

Diffusion model is applied to image generation in 2020 (Ho, Jain, and Abbeel 2020). It generates images through an iterative denoising process. The detailed theoretical derivation of diffusion models is introduced in Appendix B. While diffusion models have generated high-quality images, the lengthy iterative denoising process and complex neural networks hinder their applications in real-world scenarios. Recently, numerous methods have been proposed to reduce the lengthy denoising process. (Nichol and Dhariwal 2021) shortens the denoising steps by adjusting variance schedule; (Song, Meng, and Ermon 2020; Zhang, Tao, and Chen 2022) generalizes diffusion process to a non-Markovian process with fewer denoising steps by modifying denoising

equations; (Lu et al. 2022; Watson et al. 2022) use high-order solvers to approximate diffusion generation. These approaches have achieved significant success, but they involve expensive retraining or complex computations. In contrast, we focus on the complex neural networks, accelerating diffusion models at each denoising step with a PTQ method.

Post-Training Quantization

Post-training quantization transforms the floating-point value x of weights and activations to quantized value \hat{x} using the parameters: scale factor s and zero point z . The uniform quantizer used in our work can be formulated as:

$$\bar{x} = \text{clip} \left(\left\lfloor \frac{x}{s} \right\rfloor + z, 0, 2^b - 1 \right), \hat{x} = (\bar{x} - z) * s \quad (1)$$

where $\lfloor \cdot \rfloor$ represents rounding operation, the bit-width b determines the range of clipping function $\text{clip}(\cdot)$, and the \bar{x} is integer value for hardware efficiency.

To set the appropriate quantization parameters, minimizing the difference between the output before and after quantization, PTQ typically follows two processes: obtaining the calibration samples and reconstructing the model output. The calibration samples characterize the overall samples and directly determine the quantization performance. For traditional networks, related works (Hubara et al. 2021; Li et al. 2022c, 2023c) obtain them from training sets or generate them based on network information. Reconstruction process utilizes distillation techniques to align the outputs of quantized models and full-precision models. The most widely used block-wise reconstruction with loss as $L_b = \argmin_{s,z} \|O_f(x) - O_q(x)\|_2$, has demonstrated success in classification and detection networks (Xiao et al. 2023b; Li and Gu 2023; Xiao et al. 2023a; Li et al. 2023d), where $O_f(x)$ and $O_q(x)$ represent the outputs of the full-precision model and quantized model at one block, respectively.

Existing PTQ for diffusion models mainly focus on obtaining calibration samples. (Shang et al. 2023) and (Li et al. 2023b) design specific calibration samples, but they are based on observation and empirical evidence. (Wang et al. 2023) obtains calibration samples based on search algorithm, which introduces computational overhead. (So et al. 2023) introduces TDQ module to set different quantization parameters for each step. (He et al. 2023b) uses statistical methods to estimate the quantization error. Unfortunately, all these methods overlook the reconstruction, which is one of the most important processes in PTQ. Our work designs the more rational calibration samples and reconstruction method based on the properties of diffusion models to enhance the two processes of PTQ.

Method

Due to the unique temporal denoising process, previous PTQ methods suffer from severe performance degradation for diffusion models. We start by analyzing the challenges of PTQ for diffusion models and then propose our efficient methods to address these challenges.

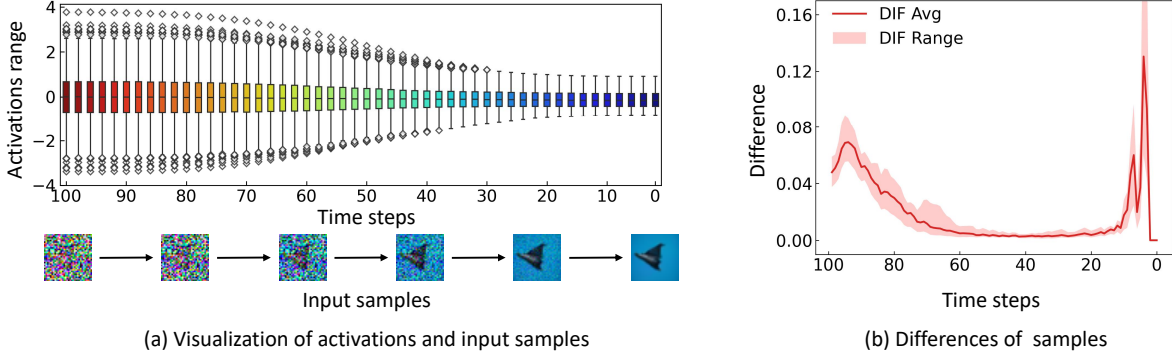


Figure 1: An overview of the challenge 1. (a) The visualization of the highly dynamic activations and input samples of diffusion models. (b) The differences of time-step samples. Here, the difference of one step sample is obtained by calculating the cosine distance between its two adjacent step samples’ feature maps and its own feature map. DIF Avg represents the average difference and DIF Range denotes the range of difference.

Challenges of PTQ for Diffusion Models

Through experiments, we find that the highly dynamic distribution of activations results in two levels of mismatch, making the quantization worse. Specifically, the time-step activations result in calibration sample level mismatch and the wide range activations result in reconstruction output level mismatch.

Challenge 1: Calibration Sample Level Mismatch. The calibration samples are expected to characterize the overall sample distribution, which helps to reduce quantization errors. For diffusion models with the temporal denoising process, at any time step t , the output sample x_t is the input of denoising network at time step $t - 1$ (as shown in Appendix B). This makes the inputs of network change with the time steps. The calibration samples for diffusion models require to align with the overall samples to reduce quantization errors at all time steps.

We run the DDIM (Song, Meng, and Ermon 2020) on CIFAR-10 (Krizhevsky, Hinton et al. 2009) with 100 denoising steps to explore the distribution of samples in the denoising process. As shown in Figure 1 (a), the highly dynamic activations at different time steps cause the input samples to change across time steps. To obtain calibration samples that match the overall sample distribution, a simple method is equally spaced sampling (sampling strategy in Q-diffusion (Li et al. 2023b)), which defaults to the same differences between samples at different time steps. Nevertheless, when feature maps are employed to characterise input samples and investigate the differences between them, as shown in Figure 1 (b), the differences between the feature maps are highly variable, indicating that equally spaced sampling is not the optimal method. Thus, at the calibration sample level, a rational sampling strategy is required.

Challenge 2: Reconstruction Output Level Mismatch.

Reconstruction is a crucial method for enhancing quantization performance, especially in low-bit cases. For single time step models, previous works have already demonstrated that block-wise reconstruction with loss as $L =$

$\min \|O_f(x) - O_q(x)\|_2$, can balance the cross-layer dependency and generalization error, resulting in superior quantization performance (Li et al. 2021, 2022b). However, when applying this approach to diffusion models, the performance is far from satisfactory.

To explore the reasons thoroughly, we quantize DDIM to 4-bits with block-wise reconstruction and examine the reconstruction performance of blocks and layers within the blocks. As shown in Figure 2, the activations in diffusion models have a wide range, making them hard to quantize. For example, in the same Residual Bottleneck Block of UNet networks, the range of activations in diffusion models is almost $3\times$ larger than that in segmentation models. To align the quantized block with the full precision block, block-wise reconstruction struggles to decrease the block loss L_b at the expense of increasing the losses (L_{m1}, L_{m2}) of the front layers. As a result, the reconstructed block is overfitted, and the front layers are underfitted. Namely, the output of reconstruction is mismatched.

Temporal Distribution Alignment Calibration

To address the calibration sample level mismatch, we attempt to extract information from the temporal network to guide the calibration samples. Feature map is a mapping of network inputs into the latent space, encompassing the feature and distribution information of input samples (Chen et al. 2021; Park and Kim 2018). In this work, we utilize the output of the middle stage of the network as a feature map because it contains high-dimensional information of the input samples (Ma, Fang, and Wang 2024). Since the diffusion model runs the network T times in one inference, we obtain feature maps from each time step to form $F = \{F_t\}_{t=1}^T$. Based on the set F , we propose *Density score* $D = \{D_t\}_{t=1}^T$, which effectively quantifies the ability of each time-step input samples to represent the overall samples. Furthermore, given that hard samples significantly influence the quantization (Li et al. 2023a), we introduce *Variety score* $V = \{V_t\}_{t=1}^T$, which quantifies the

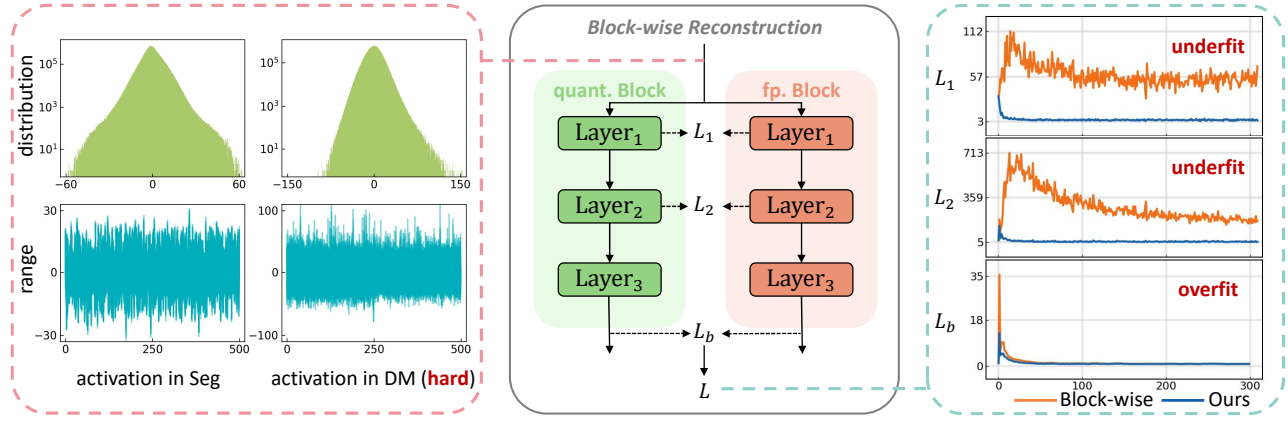


Figure 2: An overview of the challenge 2. The data and losses are obtained from the last Residual Bottleneck Block of the middle stage of the UNet network.

diversity of each time step samples. The effectiveness of the two scores is demonstrated in Appendix G. For t_{th} time step, the mathematical formulas for D_t and V_t are as follows:

$$D_t = \left| \{F_i \mid mse(F_t, F_i) < \varepsilon, F_i \in F\} \right| \quad (2)$$

$$V_t = \sum_{i=1}^T (1 - dist(F_t, F_i)) \quad (3)$$

where the function $mse(\cdot)$ calculates the MSE distances, $dist(\cdot)$ calculates the cosine similarity, and we also conduct the ablation study to demonstrate the effectiveness of the metric in Appendix F. The ε represents the distance threshold, which is set as a fixed constant for all tasks, and the function $|\cdot|$ counts the number of set elements. Namely, D_t represents the density of the feature maps F with respect to F_t , while V_t denotes the dissimilarity between F and F_t . We use the *Min-Max Scaling* to eliminate the effect of the magnitudes, obtaining the effective scores \hat{D}_t and \hat{V}_t :

$$\hat{D}_t = \frac{D_t - \min(D)}{\max(D) - \min(D)} \quad (4)$$

$$\hat{V}_t = \frac{V_t - \min(V)}{\max(V) - \min(V)} \quad (5)$$

The sum of the two scores S_t determines the proportion of samples extracted from the t_{th} time step to calibration samples. Finally, the **Temporal Distribution Alignment Calibration (TDAC)** is as follows:

$$S_t = \hat{D}_t + \lambda * \hat{V}_t \quad (6)$$

$$X_t = \frac{S_t}{\sum_{t=1}^T S_t} * N \quad (7)$$

where λ is the hyperparameter to balance these two scores, and N represents the number of calibration samples. X_t denotes samples extracted from the t_{th} time step, forming the calibration samples $X = \{X_t\}_{t=1}^T$. Consequently, as shown in Figure 3, TDAC significantly addresses the calibration sample level mismatch compared to the difference sampling strategies. The overall pipeline of TDAC is shown in Figure 4 (a).

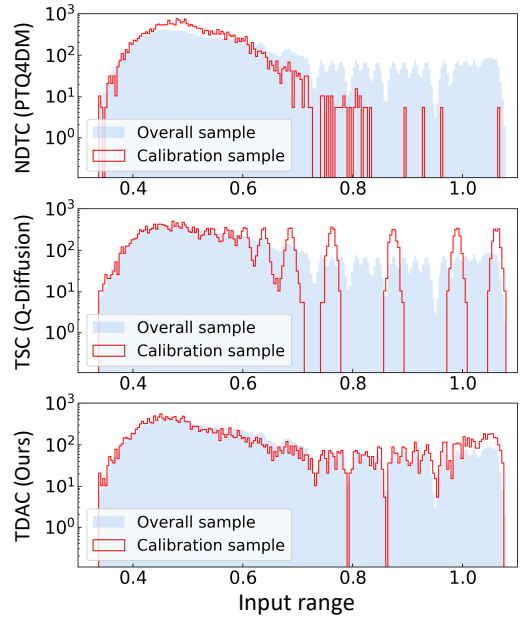


Figure 3: Visualization of the different sampling strategies. Here, the x-axis represents the distance of the samples from the geometric center of the overall samples, and the y-axis represents the number of distributed samples. The NDTC and TSC are sampling strategies for diffusion models in previous work PTQDM (Shang et al. 2023) and Q-Diffusion (Li et al. 2023b), respectively.

Fine-grained Block Reconstruction

Since previous reconstruction methods fail in aligning the output at the reconstruction level, we propose **Fine-grained Block Reconstruction (FBR)** for diffusion models. Our method modifies the loss function based on block-wise reconstruction, making it consider all layers (nn.conv, nn.linear) within the block. The new reconstruction Loss L

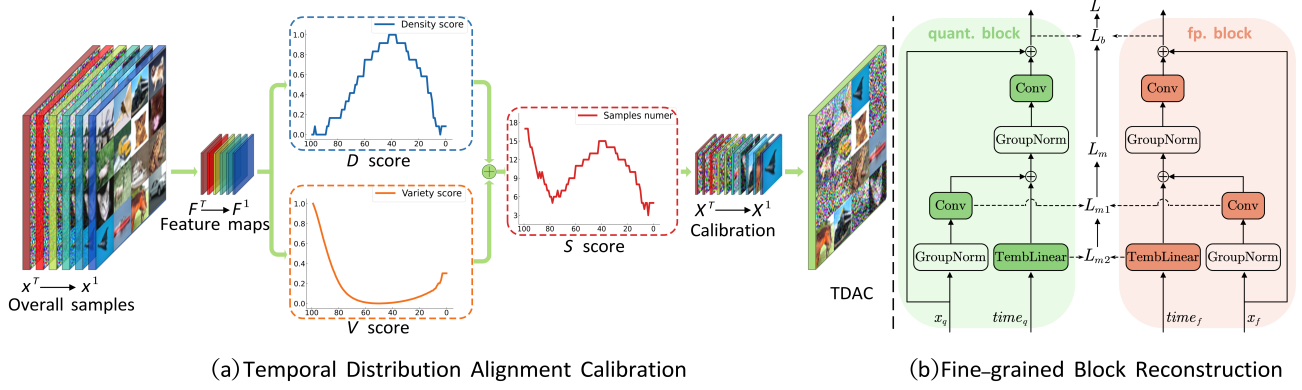


Figure 4: The overall pipeline of our method. TDAC addresses the calibration sample level mismatch by extracting information from the feature maps. FBR tackles the reconstruction output level mismatch by modifying the reconstruction loss.

Algorithm 1: Overall quantization workflow of EDA-DM

Input: Pre-trained full-precision model W_r with T denoising time steps.

Parameter: The hyperparameters λ and γ .

Output: The quantized model W_q .

- 1: **TDAC:**
 - 2: Inference W_r one time for obtaining the feature maps $F = \{F_t\}_{t=1}^T$ and input samples $x = \{x_t\}_{t=1}^T$.
 - 3: **for** $t = 1$ to T time step **do**
 - 4: Calculate the effective density score \hat{D}_t and variety score \hat{V}_t of t_{th} input sample x_t by Eq. 4 and Eq. 5.
 - 5: Calculate the sum score S_t of the x_t by Eq. 6.
 - 6: **end for**
 - 7: **for** x_t in input samples x **do**
 - 8: Calculate the proportion X_t of calibration by Eq. 7.
 - 9: Extract the X_t samples from x_t , forming the TDAC.
 - 10: **end for**
 - 11: Initialize the quantized model \hat{W}_q with TDAC.
 - 12: **FBR:**
 - 13: **for** $k = 1$ to the end Block **do**
 - 14: Calculate the block loss L_b and front $n - 1$ layers losses L_m for the k_{th} block of \hat{W}_q .
 - 15: Calculate the new loss L by Eq. 9, and update weight and activation quantizers by gradient descent algorithm.
 - 16: **end for**
 - 17: **return** W_q
-

is expressed mathematically as follows:

$$L_m = \sum_{i=1}^{n-1} L_{mi} \quad (8)$$

$$L = L_b + \gamma * L_m \quad (9)$$

where, for one block with n layers, the L consists of two parts: L_b and L_m . The former refers to the original block-wise reconstruction loss, while the latter pertains to the

losses of the layers within the block. The hyperparameter γ balances these two parts of the loss.

Note that the output of n_{th} layer is a part of the output of the block. We only use the losses from the front $n - 1$ layers to modify the reconstruction loss. For instance, the new reconstruction loss for Residual Bottleneck Block in diffusion models is shown in Figure 4 (b). Empirically, FBR effectively eliminates overfitting of reconstructed blocks and underfitting of layers within blocks, aligning quantized models with full-precision models at the reconstruction output level (as depicted in Figure 2). More importantly, it provides an efficient way to address the wide range activations in reconstruction process. To demonstrate the effect of FBR, we also visualize the reconstruction loss for all blocks in the Appendix J. The overall EDA-DM workflow is presented in Algorithm 1.

Experiments

Experimental Setup

Models and datasets. We evaluate EDA-DM for both unconditional and conditional image generation using pixel-space diffusion models (DDIMs) (Song, Meng, and Ermon 2020) and latent-space diffusion models (LDMs) (Rombach et al. 2022). For unconditional image generation, we conduct experiments using the pre-trained DDIM model on CIFAR-10 dataset, LDM-4 model on LSUN-Bedroom dataset, and LDM-8 model on LSUN-Church dataset (Yu et al. 2015). For conditional image generation, we conduct the class-guided generation experiments using LDM-4 model on ImageNet dataset (Deng et al. 2009). To demonstrate the effectiveness of our method for large models, we also conduct text-guided generation experiments with the Stable-Diffusion model on MS-COCO validation (Lin et al. 2014).

Quantization and comparison settings. For a fair quantization experiment, EDA-DM use a calibration set of 1024 samples and configure the model and reconstruction the same way as Q-Diffusion (Li et al. 2023b). we employ channel-wise quantization for weights and layer-wise quantization for activations, as it is a common setting. The notion ‘WxAy’ is employed to represent the bit-widths of

weights ‘W’ and activations ‘A’. For the experimental comparison, we compare EDA-DM with the PTQ works for diffusion models, including PTQ4DM (Shang et al. 2023), Q-Diffusion (Li et al. 2023b), and PTQD (He et al. 2023b). Since the other PTQ works, including TDQ (So et al. 2023) and ADP-DM (Wang et al. 2023), set experimental configurations differently, we also conduct experiments to compare EDA-DM with them in the Appendix C.

Metrics and evaluation. We use Fréchet Inception Distance (FID) (Heusel et al. 2017) and Sliding Fréchet Inception Distance (sFID) (Salimans et al. 2016) to evaluate the generation results. Since the generalization of Inception Score (IS) (Salimans et al. 2016) is limited, we only evaluate it for classification datasets. For text-guided experiments, we add CLIP score (Hessel et al. 2021) to evaluate the semantic relevance of the generated images to the text prompts. Furthermore, we conduct human preference evaluations to compensate for the lack of automated metrics. Following the common practice (Shang et al. 2023; Li et al. 2023b; So et al. 2023), the Stable-Diffusion generates 10,000 images, while all other models generate 50,000 images. Besides, we also calculate the Bit Operations with one denoising process and Size of models to visualize the effects of model compression and acceleration, as shown in Appendix D. All experiments are performed on one RTX A6000. The more detailed experimental implementations are showcased in Appendix A.

Unconditional Generation

We start by comparing the quantization results of EDA-DM and existing methods for unconditional image generation, as reported in Table 1. We focus on the performance of low-bit quantization to highlight the advantages of EDA-DM. At the W4A8 precision, EDA-DM achieves significant improvement with a notable 0.90 and 1.69 FID enhancement over Q-Diffusion on CIFAR-10 and LSUN-Bedroom, respectively. It also significantly improves the quantization performance on LSUN-Bedroom and LSUN-Church, with sFID reductions of 8.57 (6.59 vs. 15.16) and 4.72 (10.95 vs. 15.67) compared to PTQD, respectively. More surprisingly, even with low-bit quantization, the quantized models with EDA-DM outperform full-precision models on CIFAR-10 and LSUN-Church datasets, and narrow the FID gap to 0.61 (2.30 for Q-Diffusion) on the LSUN-Bedroom dataset. In addition, EDA-DM also achieves state-of-the-art performance compared to other PTQ works at W8A8 precision.

Conditional Generation

The experimental results for conditional image generation are reported in Table 2. For text-guided generation with W4A8 precision, EDA-DM narrows the CLIP score gap to 0.17, comparing to 0.59 and 0.88 gaps for Q-Diffusion and PTQ4DM, respectively, and it also improves the FID to 20.58. This demonstrates that EDA-DM significantly preserves the semantic information and generation quality for text-to-image large models. Besides, at the W4A8 precision, EDA-DM compresses the model size of Stable-Diffusion by 7.9 \times and reduces the Bit Operations by 31.5 \times , which effectively advances the low-latency applications of Stable-

| Task | Method | Prec. | FID↓ | sFID↓ | IS↑ |
|-----------------------------------|--------------|-------|-------------|--------------|-------------|
| CIFAR-10 32 × 32 | FP | 32/32 | 4.26 | 4.46 | 9.03 |
| | PTQ4DM* | 8/8 | 4.39 | 5.02 | 9.25 |
| | Q-Diffusion† | 8/8 | 4.06 | 4.63 | 9.38 |
| | TDQ† | 8/8 | 5.99 | - | 8.85 |
| | ADP-DM† | 8/8 | 4.24 | - | 9.07 |
| | EDA-DM | 8/8 | 3.73 | 4.47 | 9.40 |
| | PTQ4DM* | 4/8 | 5.31 | 5.33 | 9.24 |
| | Q-Diffusion† | 4/8 | 4.93 | 4.98 | 9.12 |
| | EDA-DM | 4/8 | 4.03 | 4.87 | 9.43 |
| | FP | 32/32 | 3.02 | 7.21 | - |
| LSUN Bedroom 256 × 256 | PTQ4DM* | 8/8 | 4.18 | 9.59 | - |
| | Q-Diffusion† | 8/8 | 4.40 | 8.17 | - |
| | PTQD† | 8/8 | 3.75 | 9.89 | - |
| | EDA-DM | 8/8 | 3.46 | 7.50 | - |
| | FP | 32/32 | 4.06 | 10.89 | - |
| LDM-4 steps = 200 eta = 1.0 | PTQ4DM* | 4/8 | 4.25 | 14.22 | - |
| | Q-Diffusion† | 4/8 | 5.32 | 16.82 | - |
| | PTQD† | 4/8 | 5.94 | 15.16 | - |
| | EDA-DM | 4/8 | 3.63 | 6.59 | - |
| | FP | 32/32 | 4.06 | 10.89 | - |
| LSUN Church 256 × 256 | PTQ4DM* | 8/8 | 3.98 | 13.48 | - |
| | Q-Diffusion† | 8/8 | 3.65 | 12.23 | - |
| | PTQD* | 8/8 | 4.13 | 13.89 | - |
| | EDA-DM | 8/8 | 3.83 | 10.75 | - |
| | FP | 32/32 | 4.06 | 10.89 | - |
| LDM-8 steps = 500 eta = 0.0 | PTQ4DM* | 4/8 | 4.20 | 14.87 | - |
| | Q-Diffusion† | 4/8 | 4.12 | 13.94 | - |
| | PTQD* | 4/8 | 4.33 | 15.67 | - |
| | EDA-DM | 4/8 | 4.01 | 10.95 | - |
| | FP | 32/32 | 4.06 | 10.89 | - |

Table 1: Quantization results of unconditional image generation. Here, the ‘Task’ reflects the experimental settings (dataset, resolution, model, time steps, and other hyperparameters), the ‘Prec.’ indicates the bit-widths of quantization. * denotes our implementation according to open-source codes and † represents results directly obtained by papers or rerunning open-source codes.

Diffusion in real-world scenarios, as shown in Appendix D. For class-guided generation, EDA-DM achieves significant improvements at all bit-width settings. Especially at W4A8 precision, EDA-DM improves by 0.56 FID (9.84 vs 10.40) and 6.91 sFID (5.77 vs 12.68) over PTQD, achieving loss-less compression and acceleration for diffusion models.

As assessed above, EDA-DM performs well on these automated metrics. Considering that automated metrics do not fully represent the quality of generation, we evaluate human preferences for EDA-DM by visualizing randomly generated images in Appendix I. Especially for the large text-to-image model, Stable-Diffusion, we assess the quantized models for human preferences on the convincing benchmark, DrawBench (Saharia et al. 2022). Additionally, we experimentally demonstrate the robustness of EDA-DM to different samplers, as shown in Appendix E.

| Task | Method | Prec. | FID↓ | sFID↓ | CLIP↑ |
|--|-------------------|-------|--------------|--------------|---------------|
| MS-COCO 300 × 300 Stable-Diffusion steps = 50 eta = 0.0 scale = 7.5 | FP | 32/32 | 21.96 | 33.86 | 26.88 |
| | PTQ4DM* | 8/8 | 20.48 | 33.08 | 26.79 |
| | Q-Diffusion* | 8/8 | 20.47 | 32.97 | 26.78 |
| | EDA-DM | 8/8 | 19.97 | 32.22 | 26.83 |
| | PTQ4DM* | 4/8 | 22.48 | 34.32 | 26.00 |
| | Q-Diffusion* | 4/8 | 21.96 | 33.81 | 26.29 |
| | EDA-DM | 4/8 | 20.58 | 33.08 | 26.71 |
| | FP | 32/32 | 11.69 | 7.67 | 364.73 |
| | PTQ4DM* | 8/8 | 11.57 | 9.82 | 350.24 |
| ImageNet 256 × 256 LDM-4 steps = 20 eta = 0.0 scale = 3.0 | Q-Diffusion* | 8/8 | 11.59 | 9.87 | 347.43 |
| | PTQD [†] | 8/8 | 11.94 | 8.03 | 350.26 |
| | EDA-DM | 8/8 | 11.10 | 6.95 | 353.02 |
| | PTQ4DM* | 4/8 | 13.57 | 16.06 | 323.17 |
| | Q-Diffusion* | 4/8 | 12.40 | 14.85 | 336.80 |
| | PTQD [†] | 4/8 | 10.40 | 12.68 | 344.72 |
| | EDA-DM | 4/8 | 9.84 | 5.77 | 348.75 |

Table 2: Quantization results of conditional image generation.

Ablation Study

In this section, we study the robustness of EDA-DM to the hyperparameters. we also conduct the thorough ablation study to investigate the effects of TDAC and FBR on addressing the two levels of mismatch in diffusion models. All experiments are performed on the CIFAR-10 dataset using the DDIM model with 100 time steps.

Robustness of method to hyperparameters. Our method involves two hyperparameters: λ balancing the two scores for TDAC, and γ coordinating the losses of block and layers for reconstruction. Due to time constraints, we use the quantized models to generate 10,000 images for evaluation. As shown in Figure 5, the results obtained with a wide range of λ and γ outperform the classical works PTQ4DM (FID 6.91) and Q-Diffusion (FID 6.54). This demonstrates that our method is robust to hyperparameters and easily migrates to other quantization tasks for diffusion models.

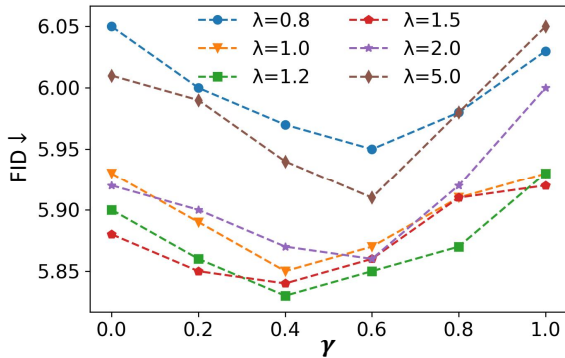


Figure 5: The quantization performance w.r.t. different hyperparameters λ and γ .

| Method | Calibration | | | |
|-------------|-------------|-------------|-------------|-------------|
| | 1024 | | 5120 | |
| | FID↓ | IS↑ | FID↓ | IS↑ |
| FP | 4.26 | 9.03 | 4.26 | 9.03 |
| NDTC | 5.31 | 9.24 | 6.48 | 9.10 |
| TSC | 4.55 | 9.36 | 4.93 | 9.12 |
| TDAC (ours) | 4.42 | 9.38 | 4.40 | 9.45 |

Table 3: Effects of TDAC with different numbers of calibration. The reconstruction method is fixed to BERCQ (Li et al. 2021), changing only the sampling strategy.

| Method | Calibration | | | |
|------------|-------------|-------------|-------------|-------------|
| | 1024 | | 5120 | |
| | FID↓ | IS↑ | FID↓ | IS↑ |
| FP | 4.26 | 9.03 | 4.26 | 9.03 |
| Layer-wise | 4.70 | 9.36 | 5.04 | 9.43 |
| Block-wise | 4.55 | 9.36 | 4.93 | 9.12 |
| FBR (ours) | 4.21 | 9.48 | 4.29 | 9.47 |

Table 4: Effects of FBR with different numbers of calibration. The calibration samples are obtained by Q-Diffusion, changing only the reconstruction method.

Effects of TDAC and FBR. We investigate the effects of TDAC and FBR on the performance improvement of quantization, respectively. As reported in Table 3, TDAC outperforms the comparison sampling strategy with different numbers of calibration samples, demonstrating that TDAC effectively addresses the calibration level mismatch. And the result of TSC with 1024 samples is instead better than the result with 5120 samples, indicating that equally spaced sampling is suboptimal and our method is rational. The results in Table 4 demonstrate that FBR balances the independence and dependence within the block layers, addresses the issue of block overfitting caused by the wide range of activations in reconstruction level. With the FBR, the quantized model even outperforms the full-precision model in W4A8 quantization. Besides, we also show the effect of merging TDAC and FBR in Appendix H.

Conclusion

In this paper, we identify the challenges of diffusion model quantization as the two levels of mismatch. Based on the insight, we propose EDA-DM, a novel PTQ method to address these issues. Specifically, at the calibration sample level, TDAC select samples based on feature maps in the temporal network to align the calibration samples with overall samples; at the reconstruction output level, FBR modifies the loss of block-wise reconstruction with the losses of layers, aligning the outputs of quantized models and full-precision models at different network granularity. Extensive experiments show that EDA-DM significantly outperforms existing methods across various models and different datasets.

References

- Chen, Y.; Liu, L.; Phonevilay, V.; Gu, K.; Xia, R.; Xie, J.; Zhang, Q.; and Yang, K. 2021. Image super-resolution reconstruction based on feature map attention mechanism. *Applied Intelligence*, 51: 4367–4380.
- Deng, J.; Dong, W.; Socher, R.; Li, L.-J.; Li, K.; and Fei-Fei, L. 2009. Imagenet: A large-scale hierarchical image database. In *2009 IEEE conference on computer vision and pattern recognition*, 248–255. Ieee.
- He, Y.; Liu, J.; Wu, W.; Zhou, H.; and Zhuang, B. 2023a. Efficientdm: Efficient quantization-aware fine-tuning of low-bit diffusion models. *arXiv preprint arXiv:2310.03270*.
- He, Y.; Liu, L.; Liu, J.; Wu, W.; Zhou, H.; and Zhuang, B. 2023b. PTQD: Accurate Post-Training Quantization for Diffusion Models. *arXiv preprint arXiv:2305.10657*.
- Hessel, J.; Holtzman, A.; Forbes, M.; Bras, R. L.; and Choi, Y. 2021. Clipscore: A reference-free evaluation metric for image captioning. *arXiv preprint arXiv:2104.08718*.
- Heusel, M.; Ramsauer, H.; Unterthiner, T.; Nessler, B.; and Hochreiter, S. 2017. Gans trained by a two time-scale update rule converge to a local nash equilibrium. *Advances in neural information processing systems*, 30.
- Ho, J.; Jain, A.; and Abbeel, P. 2020. Denoising diffusion probabilistic models. *Advances in neural information processing systems*, 33: 6840–6851.
- Hubara, I.; Nahshan, Y.; Hanani, Y.; Banner, R.; and Soudry, D. 2021. Accurate post training quantization with small calibration sets. In *International Conference on Machine Learning*, 4466–4475. PMLR.
- Krizhevsky, A.; Hinton, G.; et al. 2009. Learning multiple layers of features from tiny images.
- Li, H.; Wu, X.; Lv, F.; Liao, D.; Li, T. H.; Zhang, Y.; Han, B.; and Tan, M. 2023a. Hard Sample Matters a Lot in Zero-Shot Quantization. In *Proceedings of the IEEE/CVF Conference on Computer Vision and Pattern Recognition*, 24417–24426.
- Li, H.; Yang, Y.; Chang, M.; Chen, S.; Feng, H.; Xu, Z.; Li, Q.; and Chen, Y. 2022a. Srdiff: Single image super-resolution with diffusion probabilistic models. *Neurocomputing*, 479: 47–59.
- Li, X.; Liu, Y.; Lian, L.; Yang, H.; Dong, Z.; Kang, D.; Zhang, S.; and Keutzer, K. 2023b. Q-diffusion: Quantizing diffusion models. In *Proceedings of the IEEE/CVF International Conference on Computer Vision*, 17535–17545.
- Li, Y.; Gong, R.; Tan, X.; Yang, Y.; Hu, P.; Zhang, Q.; Yu, F.; Wang, W.; and Gu, S. 2021. Brecq: Pushing the limit of post-training quantization by block reconstruction. *arXiv preprint arXiv:2102.05426*.
- Li, Z.; Chen, M.; Xiao, J.; and Gu, Q. 2023c. PSAQ-ViT V2: Toward Accurate and General Data-Free Quantization for Vision Transformers. *IEEE Transactions on Neural Networks and Learning Systems*.
- Li, Z.; and Gu, Q. 2023. I-vit: Integer-only quantization for efficient vision transformer inference. In *Proceedings of the IEEE/CVF International Conference on Computer Vision*, 17065–17075.
- Li, Z.; Ma, L.; Chen, M.; Xiao, J.; and Gu, Q. 2022b. Patch similarity aware data-free quantization for vision transformers. In *European Conference on Computer Vision*, 154–170. Springer.
- Li, Z.; Ma, L.; Long, X.; Xiao, J.; and Gu, Q. 2022c. Dual-discriminator adversarial framework for data-free quantization. *Neurocomputing*, 511: 67–77.
- Li, Z.; Xiao, J.; Yang, L.; and Gu, Q. 2023d. Repq-vit: Scale reparameterization for post-training quantization of vision transformers. In *Proceedings of the IEEE/CVF International Conference on Computer Vision*, 17227–17236.
- Lin, T.-Y.; Maire, M.; Belongie, S.; Hays, J.; Perona, P.; Ramanan, D.; Dollár, P.; and Zitnick, C. L. 2014. Microsoft coco: Common objects in context. In *Computer Vision—ECCV 2014: 13th European Conference, Zurich, Switzerland, September 6–12, 2014, Proceedings, Part V 13*, 740–755. Springer.
- Lu, C.; Zhou, Y.; Bao, F.; Chen, J.; Li, C.; and Zhu, J. 2022. Dpm-solver++: Fast solver for guided sampling of diffusion probabilistic models. *arXiv preprint arXiv:2211.01095*.
- Lugmayr, A.; Danelljan, M.; Romero, A.; Yu, F.; Timofte, R.; and Van Gool, L. 2022. Repaint: Inpainting using denoising diffusion probabilistic models. In *Proceedings of the IEEE/CVF Conference on Computer Vision and Pattern Recognition*, 11461–11471.
- Ma, X.; Fang, G.; and Wang, X. 2024. Deepcache: Accelerating diffusion models for free. In *Proceedings of the IEEE/CVF Conference on Computer Vision and Pattern Recognition*, 15762–15772.
- Nichol, A.; Dhariwal, P.; Ramesh, A.; Shyam, P.; Mishkin, P.; McGrew, B.; Sutskever, I.; and Chen, M. 2021. Glide: Towards photorealistic image generation and editing with text-guided diffusion models. *arXiv preprint arXiv:2112.10741*.
- Nichol, A. Q.; and Dhariwal, P. 2021. Improved denoising diffusion probabilistic models. In *International Conference on Machine Learning*, 8162–8171. PMLR.
- Niu, C.; Song, Y.; Song, J.; Zhao, S.; Grover, A.; and Ermon, S. 2020. Permutation invariant graph generation via score-based generative modeling. In *International Conference on Artificial Intelligence and Statistics*, 4474–4484. PMLR.
- Ozbey, M.; Dalmaz, O.; Dar, S. U.; Bedel, H. A.; Ozturk, S.; Gungor, A.; and Cukur, T. 2023. Unsupervised Medical Image Translation with Adversarial Diffusion Models. *IEEE Transactions on Medical Imaging*.
- Park, K.; and Kim, D.-H. 2018. Accelerating image classification using feature map similarity in convolutional neural networks. *Applied Sciences*, 9(1): 108.
- Phung, H.; Dao, Q.; and Tran, A. 2023. Wavelet diffusion models are fast and scalable image generators. In *Proceedings of the IEEE/CVF Conference on Computer Vision and Pattern Recognition*, 10199–10208.
- Rombach, R.; Blattmann, A.; Lorenz, D.; Esser, P.; and Ommer, B. 2022. High-resolution image synthesis with latent diffusion models. In *Proceedings of the IEEE/CVF conference on computer vision and pattern recognition*, 10684–10695.

- Ronneberger, O.; Fischer, P.; and Brox, T. 2015. U-net: Convolutional networks for biomedical image segmentation. In *Medical Image Computing and Computer-Assisted Intervention–MICCAI 2015: 18th International Conference, Munich, Germany, October 5-9, 2015, Proceedings, Part III* 18, 234–241. Springer.
- Saharia, C.; Chan, W.; Saxena, S.; Li, L.; Whang, J.; Denton, E. L.; Ghasemipour, K.; Gontijo Lopes, R.; Karagol Ayan, B.; Salimans, T.; et al. 2022. Photorealistic text-to-image diffusion models with deep language understanding. *Advances in neural information processing systems*, 35: 36479–36494.
- Salimans, T.; Goodfellow, I.; Zaremba, W.; Cheung, V.; Radford, A.; and Chen, X. 2016. Improved techniques for training gans. *Advances in neural information processing systems*, 29.
- Shang, Y.; Yuan, Z.; Xie, B.; Wu, B.; and Yan, Y. 2023. Post-training quantization on diffusion models. In *Proceedings of the IEEE/CVF Conference on Computer Vision and Pattern Recognition*, 1972–1981.
- So, J.; Lee, J.; Ahn, D.; Kim, H.; and Park, E. 2023. Temporal Dynamic Quantization for Diffusion Models. *arXiv preprint arXiv:2306.02316*.
- So, J.; Lee, J.; Ahn, D.; Kim, H.; and Park, E. 2024. Temporal dynamic quantization for diffusion models. *Advances in Neural Information Processing Systems*, 36.
- Song, J.; Meng, C.; and Ermon, S. 2020. Denoising diffusion implicit models. *arXiv preprint arXiv:2010.02502*.
- Wang, C.; Wang, Z.; Xu, X.; Tang, Y.; Zhou, J.; and Lu, J. 2023. Towards Accurate Data-free Quantization for Diffusion Models. *arXiv preprint arXiv:2305.18723*.
- Watson, D.; Chan, W.; Ho, J.; and Norouzi, M. 2022. Learning fast samplers for diffusion models by differentiating through sample quality. *arXiv preprint arXiv:2202.05830*.
- Xiao, J.; Jiang, H.; Li, Z.; and Gu, Q. 2023a. DCIFPN: Deformable cross-scale interaction feature pyramid network for object detection. *IET Image Processing*.
- Xiao, J.; Li, Z.; Yang, L.; and Gu, Q. 2023b. Patch-wise Mixed-Precision Quantization of Vision Transformer. *arXiv preprint arXiv:2305.06559*.
- Xu, M.; Zhao, M.; Yu, S.; Zheng, X.; Wu, N.; and Liu, L. 2021. Rounding Shift Channel Post-Training Quantization using Layer Search. In *2021 4th International Conference on Artificial Intelligence and Big Data (ICAIBD)*, 545–549. IEEE.
- Yu, F.; Seff, A.; Zhang, Y.; Song, S.; Funkhouser, T.; and Xiao, J. 2015. Lsun: Construction of a large-scale image dataset using deep learning with humans in the loop. *arXiv preprint arXiv:1506.03365*.
- Zhang, L.; Rao, A.; and Agrawala, M. 2023. Adding conditional control to text-to-image diffusion models. In *Proceedings of the IEEE/CVF International Conference on Computer Vision*, 3836–3847.
- Zhang, Q.; Tao, M.; and Chen, Y. 2022. gDDIM: Generalized denoising diffusion implicit models. *arXiv preprint arXiv:2206.05564*.
- Zhang, Y.; Huang, N.; Tang, F.; Huang, H.; Ma, C.; Dong, W.; and Xu, C. 2023. Inversion-based style transfer with diffusion models. In *Proceedings of the IEEE/CVF Conference on Computer Vision and Pattern Recognition*, 10146–10156.

EDA-DM: Supplementary Materials

Supplementary material introduction

In this supplementary material, we present the correlative introductions and some experiments mentioned in the paper. The following items are provided:

- Detailed experimental implementations for all experiments in Appendix A.
- Brief introduction to diffusion model in Appendix B.
- Comparison with other PTQ frameworks in Appendix C.
- Visualisation of model compression and acceleration in Appendix D.
- Ablation study of samplers in Appendix E.
- Selection of metrics for two scores in Appendix F.
- Effectiveness of two scores in Appendix G.
- Effect of methods combination in Appendix H.
- Human preference evaluation in Appendix I.
- Specific implementation and performance of FBR in Appendix J.

A: Detailed experimental implementations

In this section, we present detailed experimental implementations, including the pre-training models, experimental settings, and evaluation.

For pre-training models, we use DDIM¹ models and LDM² models for the experiments obtained from the official website. For text-guided generation with Stable-Diffusion, we use the CompVis codebase³ and its v1.4 checkpoint.

The LDM model consists of a diffusion model and a decoder model. Like the previous works (Li et al. 2023b; Wang et al. 2023; He et al. 2023b), we focus only on the diffusion model and does not quantize the decoder model. For quantization experiments, we employ channel-wise asymmetric quantization for weights and layer-wise asymmetric quantization for activations, following the same approach as Q-Diffusion (Li et al. 2023b). The weight and activation quantization ranges are initially determined by minimizing values error, and then trained via gradient descent to minimize reconstruction loss, as in methods like BRECQ (Li et al. 2021). In the reconstruction training, we set the calibration samples to 1024 and the training batch to 32 for all experiments. However, for the Stable-Diffusion model, we adjust the reconstruction calibration samples to 256 and the training batch to 2 due to time and memory source constraints.

For experimental evaluation, we use open-source tool *pytorch-OpCounter*⁴ to calculate the Size and Bops of models before and after quantization. And following the quantization setting, we only calculate the diffusion model part, not the decoder and encoder parts. We use the ADM’s TensorFlow evaluation suite *guided-diffusion*⁵ to evaluate FID, sFID, and IS, and use the open-source code *clip-score*⁶ to evaluate CLIP scores. To ensure fair evaluation, the class-guided models generate samples that include all ImageNet categories, and the number of samples for each category is the same. As per the standard practice (Nichol et al. 2021), we employ the zero-shot approach to evaluate Stable-Diffusion on COCO-val for the text-guided experiments, resizing the generated 512×512 images and validation images in 300×300 with the center cropping to evaluate FID score and using text prompts from COCO-val to evaluate CLIP score.

B: Diffusion Model

The diffusion model consists of two processes. As shown in Figure 6, the forward diffusion process gradually adds Gaussian noise to real data $x_0 \sim q(x_0)$ for T times, which is a Markov process:

$$q(x_t | x_{t-1}) = \mathcal{N}(x_t; \sqrt{1 - \beta_t}x_{t-1}, \beta_t \mathbf{I}) \quad (10)$$

where β_t is the hyperparameter. When T is sufficiently large $T \sim \infty$, x_T approximates an isotropic Gaussian distribution $x_T \sim \mathcal{N}(0, \mathbf{I})$.

The denoising process removes the noise from the input x_T to generate high-quality images. Since $q(x_{t-1} | x_t)$ relies on $q(x_0)$, which is unavailable, diffusion model approach it by learning a Gaussian distribution:

$$p_\theta(x_{t-1} | x_t) = \mathcal{N}(x_{t-1}; \mu_\theta(x_t, t), \Sigma_\theta(x_t, t)) \quad (11)$$

¹<https://github.com/ermongroup/ddim>

²<https://github.com/CompVis/latent-diffusion>

³<https://github.com/CompVis/stable-diffusion>

⁴<https://github.com/Lyken17/pytorch-OpCounter>

⁵<https://github.com/openai/guided-diffusion>

⁶<https://github.com/Taited/clip-score>

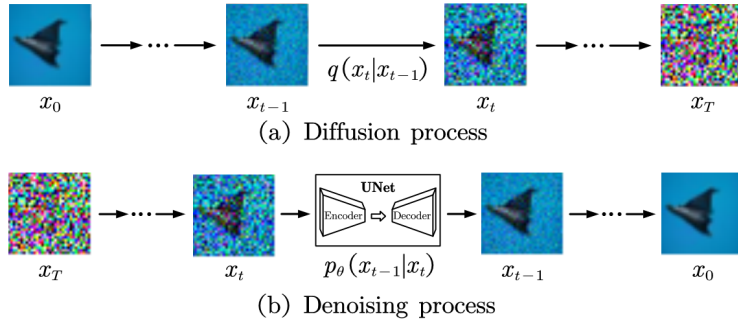


Figure 6: Brief illustration of Diffusion Model. In the training, the diffusion process (a) gradually adds noise to the real data x_0 . In the inference, the denoising process (b) iteratively uses the UNet network to denoise noise from Gaussian data x_T .

where the variance $\Sigma_\theta(x_t, t)$ can be fixed as a constant schedule σ_t to make the training stable. And with the reparameterization trick (Ho, Jain, and Abbeel 2020), the mean $\mu_\theta(x_t, t)$ can be formulated as:

$$\mu_\theta(x_t, t) = \frac{1}{\sqrt{\alpha_t}}(x_t - \frac{\beta_t}{\sqrt{1 - \bar{\alpha}_t}}\epsilon_\theta(x_t, t)) \quad (12)$$

where $\alpha_t = 1 - \beta_t$, $\bar{\alpha}_t = \prod_{k=1}^t \alpha_k$. Finally, the denoising process generates x_{t-1} by predicting $\epsilon_\theta(x_t, t)$ through the UNet (Ronneberger, Fischer, and Brox 2015) noise estimation network:

$$x_{t-1} = \frac{1}{\sqrt{\alpha_t}}(x_t - \frac{\beta_t}{\sqrt{1 - \bar{\alpha}_t}}\epsilon_\theta(x_t, t)) + \sigma_t z \quad (13)$$

where $z = \mathcal{N}(0, \mathbf{I})$.

| Task | Method | Calib. | Prec. (W/A) | FID↓ |
|--------------------------------------|--------|--------|-------------|--------------|
| CIFAR-10 DDIM steps = 100 | FP | - | 32/32 | 4.26 |
| | TDQ | 5120 | 8/8 | 5.99 |
| | ADP-DM | 1024 | 8/8 | 4.24 |
| | EDA-DM | 1024 | 8/8 | 3.73 |
| LSUN-Bedroom LDM-4 steps = 100 | FP | - | 32/32 | 3.43 |
| | ADP-DM | 1024 | 8/8 | 3.88 |
| | EDA-DM | 1024 | 8/8 | 3.29 |
| LSUN-Church LDM-8 steps = 100 | FP | - | 32/32 | 4.04 |
| | TDQ | 5120 | 8/8 | 3.89 |
| | ADP-DM | 1024 | 8/8 | 4.02 |
| | EDA-DM | 1024 | 8/8 | 3.83 |
| ImageNet LDM-4 steps = 100 | FP | - | 32/32 | 11.89 |
| | ADP-DM | 1024 | 8/8 | 11.58 |
| | EDA-DM | 1024 | 8/8 | 10.45 |

Table 5: The results of TDQ, ADP-DM, and EDA-DM. Here, the “Calib.” presents the number of calibration samples.

| Task | Method | Calib. | Prec. (W/A) | FID↓ |
|--------------------------------------|--------|--------|-------------|--------------|
| LSUN-Bedroom LDM-4 steps = 200 | FP | - | 32/32 | 3.02 |
| | PTQD | 1024 | 8/8 | 3.75 |
| | EDA-DM | 1024 | 8/8 | 3.46 |
| | PTQD | 1024 | 4/8 | 5.94 |
| | EDA-DM | 1024 | 4/8 | 3.63 |
| LSUN-Church LDM-8 steps = 200 | FP | - | 32/32 | 3.90 |
| | PTQD | 1024 | 8/8 | 6.40 |
| | EDA-DM | 1024 | 8/8 | 3.92 |
| | PTQD | 1024 | 4/8 | 7.33 |
| | EDA-DM | 1024 | 4/8 | 4.25 |
| ImageNet LDM-4 steps = 20 | FP | - | 32/32 | 11.69 |
| | PTQD | 1024 | 8/8 | 11.94 |
| | EDA-DM | 1024 | 8/8 | 11.10 |
| | PTQD | 1024 | 4/8 | 10.40 |
| | EDA-DM | 1024 | 4/8 | 9.84 |

Table 6: The results of PTQD and EDA-DM.

C: Comparison with other PTQ frameworks

We set the experimental configurations the same as the other PTQ works (Wang et al. 2023; So et al. 2023; He et al. 2023b), comparing EDA-DM with them at the W4A8 and W8A8 precision. TDQ (So et al. 2023) sets different quantization parameters for each time steps through an additional neural network module, while obviously for different diffusion models the module needs to be retrained. ADP-DM (Wang et al. 2023) uses a differentiable search algorithms to set group-wise quantization functions for all time steps, which introduces complex computations. PTQD (He et al. 2023b) categorizes the quantization errors and compensates for them using statistical methods. We evaluated EDA-DM on the different models settings employed

in these works. Since TDQ and ADP-DM do not have experiments with the W4A8 precision setting and they do not open the code, we compare with them at W8A8 precision, and the comparison results are reported in Table 5. We compare with PTQD at both W4A8 and W8A8 precision, as shown in Table 6. All of the experiments on ImageNet dataset are class-guided image generation and the other experiments are unconditional image generation.

The experimental results show that, applying EDA-DM to models with different time steps and hyperparameters, all of them achieve the state-of-the-art results. And EDA-DM improves the two basis processes of PTQ without introducing any computational overhead or complex computations in the inference.

| Model | Method | Prec. (W/A) | TBops | Size (MB) | FID↓ |
|-----------------------------|-------------|-------------|-------|-----------|--------------|
| DDIM CIFAR-10 | FP | 32/32 | 6.2 | 143.0 | 4.26 |
| | Q-Diffusion | 8/8 | 0.4 | 35.9 | 4.06 |
| | EDA-DM | 8/8 | 0.4 | 35.9 | 3.73 |
| | Q-Diffusion | 4/8 | 0.2 | 18.1 | 4.93 |
| | EDA-DM | 4/8 | 0.2 | 18.1 | 4.03 |
| | FP | 32/32 | 98.4 | 1317.4 | 3.02 |
| LDM-4 LSUN-Bedroom | Q-Diffusion | 8/8 | 6.1 | 330.1 | 4.40 |
| | EDA-DM | 8/8 | 6.1 | 330.1 | 3.46 |
| | Q-Diffusion | 4/8 | 3.2 | 165.5 | 5.32 |
| | EDA-DM | 4/8 | 3.2 | 165.5 | 3.63 |
| | FP | 32/32 | 19.1 | 1514.5 | 4.06 |
| | Q-Diffusion | 8/8 | 1.2 | 379.5 | 3.65 |
| LDM-8 LSUN-Church | EDA-DM | 8/8 | 1.2 | 379.5 | 3.83 |
| | Q-Diffusion | 4/8 | 0.7 | 190.3 | 4.12 |
| | EDA-DM | 4/8 | 0.7 | 190.3 | 4.01 |
| | FP | 32/32 | 694.3 | 4112.5 | 21.96 |
| | Q-Diffusion | 8/8 | 43.8 | 1029.7 | 20.47 |
| | EDA-DM | 8/8 | 43.8 | 1029.7 | 19.97 |
| Stable-Diffusion MS-COCO | Q-Diffusion | 4/8 | 22.2 | 515.9 | 21.96 |
| | EDA-DM | 4/8 | 22.2 | 515.9 | 20.58 |
| | FP | 32/32 | 204.6 | 1824.6 | 11.69 |
| | Q-Diffusion | 8/8 | 12.9 | 457.1 | 11.59 |
| | EDA-DM | 8/8 | 12.9 | 457.1 | 11.50 |
| | Q-Diffusion | 4/8 | 6.5 | 229.2 | 12.40 |
| LDM-4 ImageNet | EDA-DM | 4/8 | 6.5 | 229.2 | 9.84 |

Table 7: The effect of model compression and acceleration. Here, “TBops” is the unit of the number of bit operations.

D: Visualisation of model compression and acceleration

We evaluate the effect of model compression and acceleration by comparing the size and number of bit operations of models before and after quantization. More specifically, we utilize the open-source tool pytorch-OpCounter to calculate the bit operations with one denoising process and size of models. The results are reported in Table 7. At the W4A8 quantization, EDA-DM achieves $7.9\times$ compression and nearly $31\times$ reduction in bit operations for diffusion models. Especially for Stable-Diffusion, EDA-DM compresses the model size from 4112.5 MB to 515.9 MB, significantly facilitating the real-world applications of large text-to-image models. Additionally, EDA-DM, like the standard PTQ work Q-Diffusion, does not introduce any additional computations.

E: Ablation study of samplers

In this section, we perform ablation experiments to demonstrate the robustness of EDA-DM to different samplers. As reported in Table 8, EDA-DM outperforms existing methods across different samplers, including DDIMSampler, PLMSampler, and DPM-SolverSampler. With W4A8 quantization, EDA-DM improves FID by 0.56, 0.10, and 0.36 compared to PTQD at DDIMSampler, PLMSampler, and DPMSolverSampler, respectively. Moreover, EDA-DM shows superior IS metrics at different precision. This demonstrates the robustness of EDA-DM for different samplers.

| Task | Method | Prec. | FID↓ | sFID↓ | IS↑ |
|--------------------------------------|-------------|-------|--------------|-------------|---------------|
| LDM-4——DDIM time steps = 20 | FP | 32/32 | 11.69 | 7.67 | 364.73 |
| | Q-Diffusion | 8/8 | 11.59 | 9.87 | 347.43 |
| | PTQD | 8/8 | 11.94 | 8.03 | 350.26 |
| | Ours | 8/8 | 11.10 | 6.95 | 353.02 |
| | Q-Diffusion | 4/8 | 12.40 | 14.85 | 336.80 |
| | PTQD | 4/8 | 10.40 | 12.68 | 344.72 |
| | Ours | 4/8 | 9.84 | 5.77 | 348.75 |
| | FP | 32/32 | 11.71 | 6.08 | 379.19 |
| | Q-Diffusion | 8/8 | 11.25 | 7.75 | 360.49 |
| LDM-4——PLMS time steps = 20 | PTQD | 8/8 | 11.05 | 7.42 | 361.13 |
| | Ours | 8/8 | 10.91 | 7.61 | 363.53 |
| | Q-Diffusion | 4/8 | 11.27 | 5.74 | 358.13 |
| | PTQD | 4/8 | 10.84 | 5.96 | 357.66 |
| | Ours | 4/8 | 10.74 | 5.68 | 359.60 |
| | FP | 32/32 | 11.44 | 6.85 | 373.12 |
| | Q-Diffusion | 8/8 | 10.78 | 7.15 | 342.64 |
| | PTQD | 8/8 | 10.66 | 6.73 | 348.22 |
| | Ours | 8/8 | 10.58 | 6.55 | 352.51 |
| LDM-4——DPM-Solver time steps = 20 | Q-Diffusion | 4/8 | 9.36 | 6.86 | 351.00 |
| | PTQD | 4/8 | 8.88 | 6.73 | 354.94 |
| | Ours | 4/8 | 8.52 | 6.45 | 360.85 |

Table 8: The performance of EDA-DM on different samplers.

F: Selection of metrics for two scores

In this section, we conduct ablation experiments to explore the impact of the metrics on two scores. Following the experience of PTQ4DM, we utilize the Mean Squared Error (MSE) metric to derive the density score since the density distribution is highly correlated with quantization calibration. For the diversity score, we employ MSE, Cosine similarity, Peak Signal-to-Noise Ratio (PSNR), and Structural Similarity Index (SSIM) to assess the similarity between feature maps. As reported in Table 9, the Cosine metric is better. Therefore, we use cosine as the metric for calculating the diversity score.

| Metrics | MSE | Cosine | PSNR | SSIM |
|---------|------|--------|------|------|
| FID↓ | 4.25 | 4.03 | 5.74 | 4.29 |

Table 9: Performance comparisons under different metrics for diversity score. Data is collected over W4A8 DDIM model on CIFAR-10.

G: Effectiveness of two scores

We propose two scores based on the latent space feature-maps of the diffusion model. The Density score D is to evaluate the ability of different time step samples to represent the overall sample distribution. A high D_t score denotes that the features of the sample at the t_{th} time step have small differences to the features of overall sample. This indicates that the samples have high density in the overall sample. Therefore, to approximate the overall sample distribution, more samples need to be taken at that time step. The Variety score V is to evaluate the hard-to-quantize property of sample at different time steps. Given that hard samples significantly influence quantization, it is necessary to add hard samples to the calibration. Experimentally, we find that the hard-to-quantize property of the sample is strongly correlated with its feature-map diversity, as shown in Figure 7 (b). So we evaluate the properties of hard samples by the diversity of feature maps. A high V_t score represents the more difficulty of quantizing the sample at the t_{th} time step. To make the quantization more robust, more samples need to be taken at that time step.

It is likely not feasible to demonstrate the effectiveness of the two scores separately through the performance of quantized model, since samples matched the density distribution and hard samples are both important for quantization. So we demonstrate the effectiveness of the two scores separately through the existing arguments and intuitive experiment. As shown in Figure 7, the D score is consistent with the $NDTC$ curve (Shang et al. 2023), which is a sampling curve artificially designed through

extensive experimentation to fit the overall sample distribution. This shows that D can reasonably represent the distribution of the overall sample. The V score is consistent with the quantization $Loss$ curve, which demonstrates that V can effectively find hard samples through the diversity of feature maps.

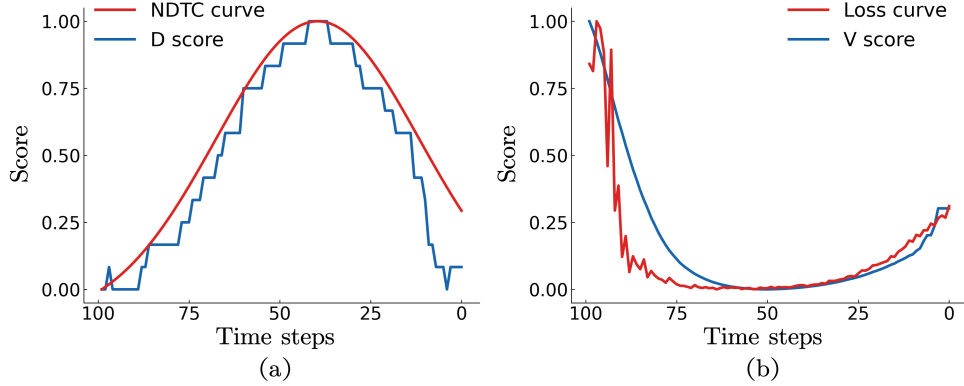


Figure 7: Demonstration of the effectiveness of two scores. The D and V scores are obtained by the DDIM on CIFAR-10 with 100 time steps. The NDTC curve is the efficient normally distributed sampling setup for the PTQ4DM (Shang et al. 2023) on CIFAR-10 tasks. The Loss curve is the MSE error of the network output before and after quantization at different time steps.

H: Effect of methods combination

In the section 4.4, the ablation studies demonstrate that our methods outperform the previous methods in both the sample strategy and reconstruction method. In this section, we conduct the same DDIM experiments to analyze the combination effect of our methods. The experimental results in Figure 8 show that our methods achieve better results when combined. With the W8A8 precision setting, the quantized model achieves an 0.5 (3.78 vs. 4.28) FID reduction with only adding the TDAC. And the effect of FBR is more obvious on W4A8 quantization, achieving an FID of 4.03.

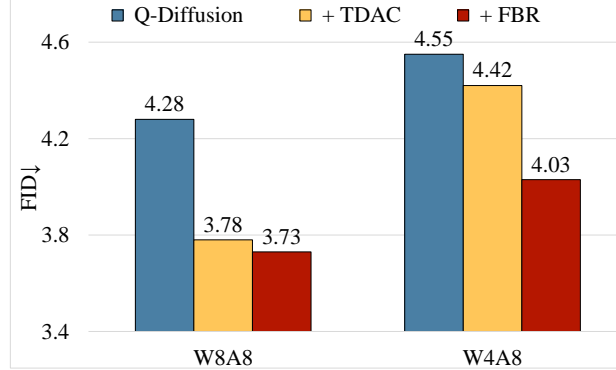


Figure 8: The combination effect of our methods based on the Q-Diffusion (Li et al. 2023b) baseline.

I: Human preference evaluation

In this section, we conduct a human preference evaluation by visualizing the random samples generated by the different quantized models. The results are shown in Figure 11 (CIFAR), 12 (LSUN-Bedroom), 13 (LSUN-church), 14 (ImageNet), and 15 (COCO). As can be seen, EDA-DM outperforms previous methods in terms of image quality, fidelity, and diversity. For the large text-to-image model, we use the DrawBench benchmark to evaluate human performance. As shown in Figure 16, due to the low-bit quantization, the quantized model cannot generate images exactly the same as the full-precision model. However, when compared to other methods, EDA-DM significantly preserves the semantic information and generation quality. Additionally, we use an open-source *aesthetic predictor*⁷ to evaluate Aesthetic Score ↑, mimicking human preference assessment of the generated images. As reported in Table 10, EDA-DM has a better aesthetic representation compared to Q-Diffusion,

⁷<https://github.com/shunk031/simple-aesthetics-predictor>

which demonstrates that the quantized model with our method enable to generates images that are more aesthetically pleasing to humans.

| Method | LSUN-Bedroom | LSUN-Church | DrawBench |
|-------------|--------------|-------------|-----------|
| FP | 5.91 | 5.88 | 5.80 |
| Q-Diffusion | 5.82 | 5.75 | 5.60 |
| EDA-DM | 5.87 | 5.80 | 5.66 |

Table 10: Aesthetic assessment of the different quantized models with W4A8 quantization.

J: Specific implementation and performance of FBR

Based on the analysis in section 3.1 **Challenge 2**, previous reconstruction methods lead to overfitting of the diffusion model network blocks. In this section, we introduce the specific implementations and performance of FBR on network blocks. Since the output of the last layer of a block is typically part of the block output, FBR only considers the losses of the front $n - 1$ layers to modify the reconstruction loss. Taking the DDIM model with UNet framework as an example, the blocks includes Residual Bottleneck Block and Transformer Block. The former sequentially contains the `conv1`, `temb_proj`, and `conv2` layers in the down stage of network, and it additionally contains the `nin_shortcut` layer in the up stage of network. Due to the outputs of `conv2` and `nin_shortcut` are both part of the block output, Residual Bottleneck Block modifies the reconstruction loss by adding the losses of `conv1` and `temb_proj` layers. Transformer Blocks sequentially contains the `q`, `k`, `v`, and `proj_out` layers, and the reconstruction loss is modified by the losses of `q`, `k`, `v` layers. With the W4A8 precision setting, the reconstruction losses before and after modification of Transformer Blocks and Residual Bottleneck Blocks in DDIM model on CIFAR-10 dataset are shown in Figure 9 and 10, respectively. FBR significantly reduces the losses of layers while maintaining the loss of block drop, effectively eliminating the overfitting of blocks.

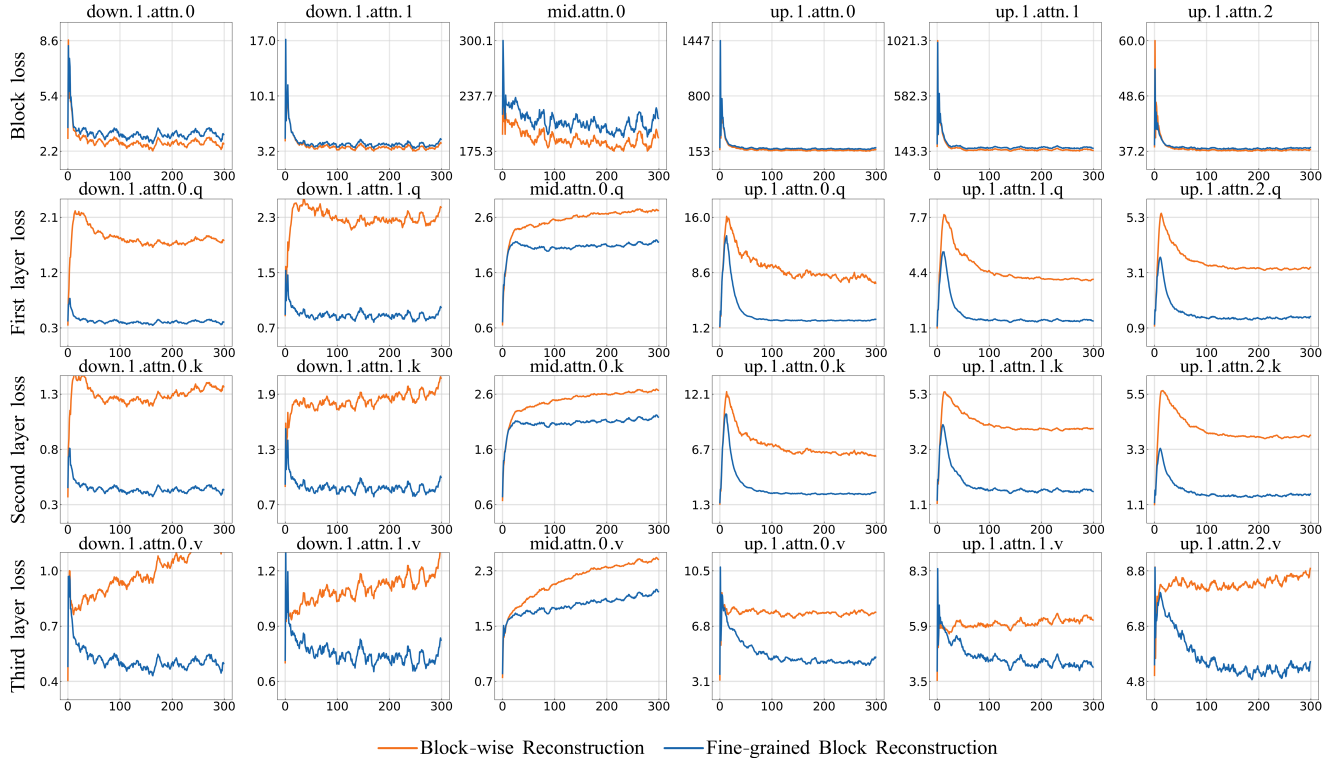


Figure 9: The reconstruction losses before and after modification of Transformer Blocks.

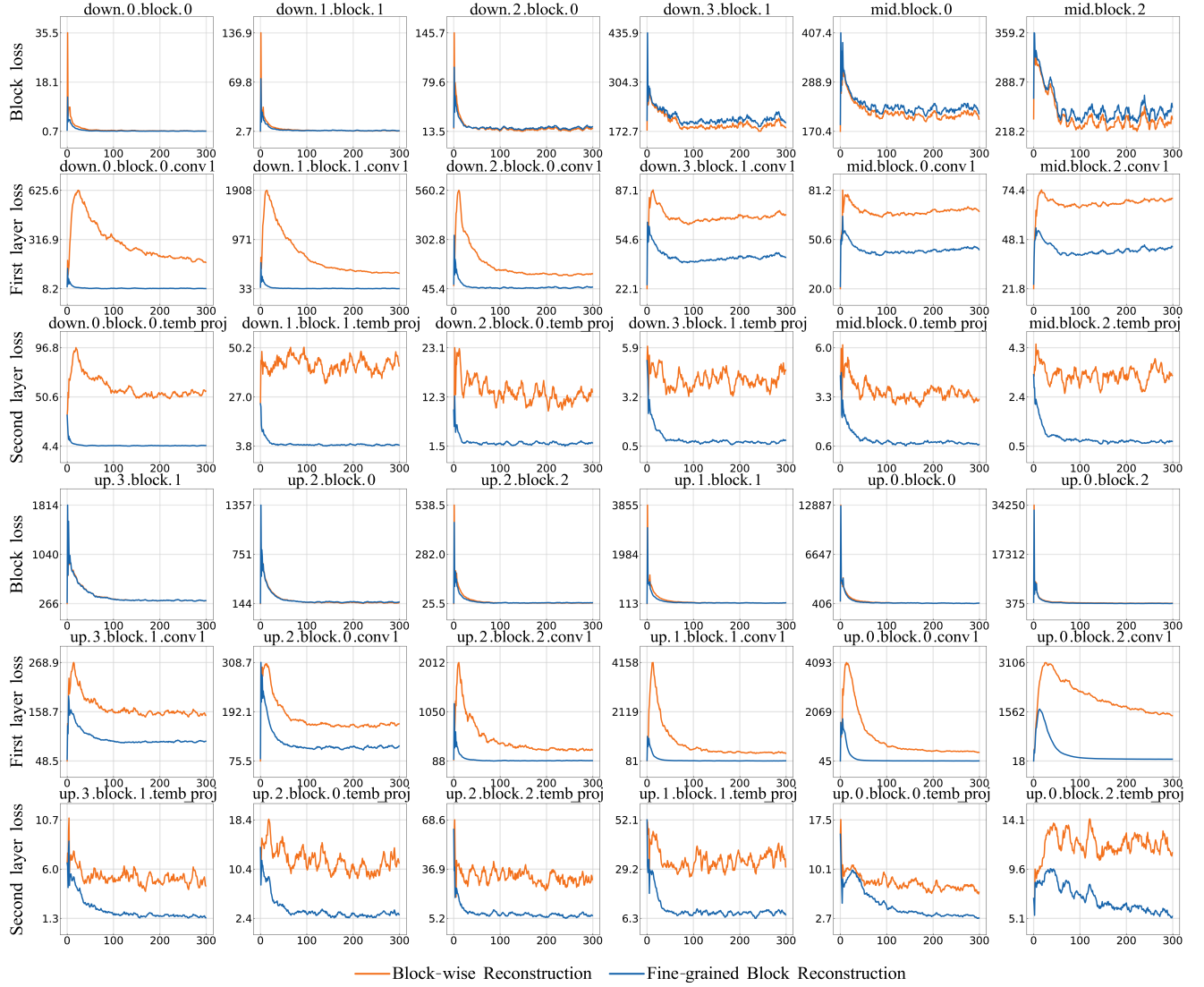


Figure 10: The reconstruction losses before and after modification of Residual Bottleneck Blocks.



Figure 11: Random samples generated by DDIM model on CIFAR dataset with W4A8 quantization.



Figure 12: Random samples generated by LDM-4 model on LSUN-Bedroom dataset with W4A8 quantization.

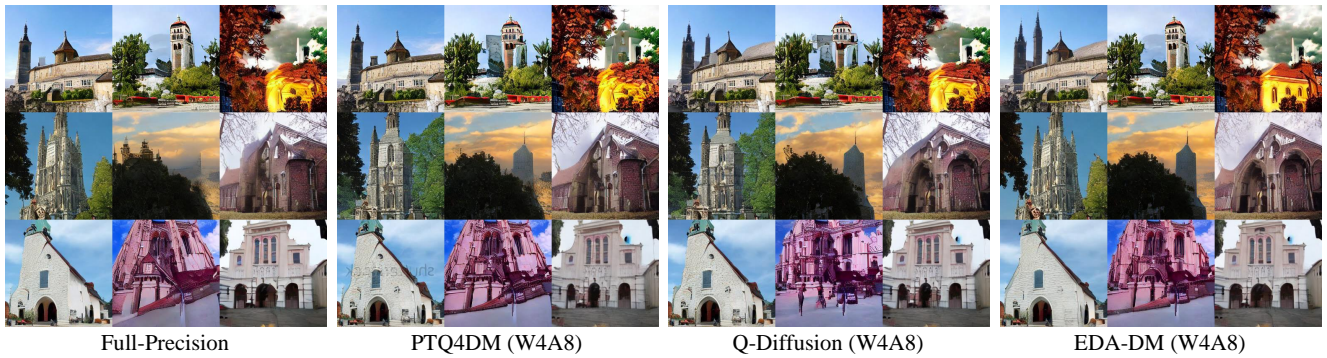


Figure 13: Random samples generated by LDM-8 model on LSUN-Church dataset with W4A8 quantization.

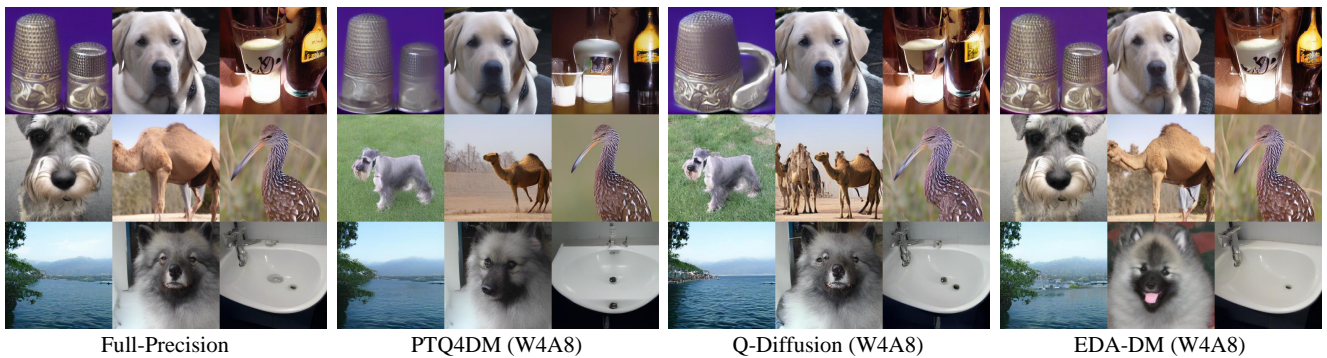


Figure 14: Random samples generated by LDM-4 model on ImageNet dataset with W4A8 quantization.

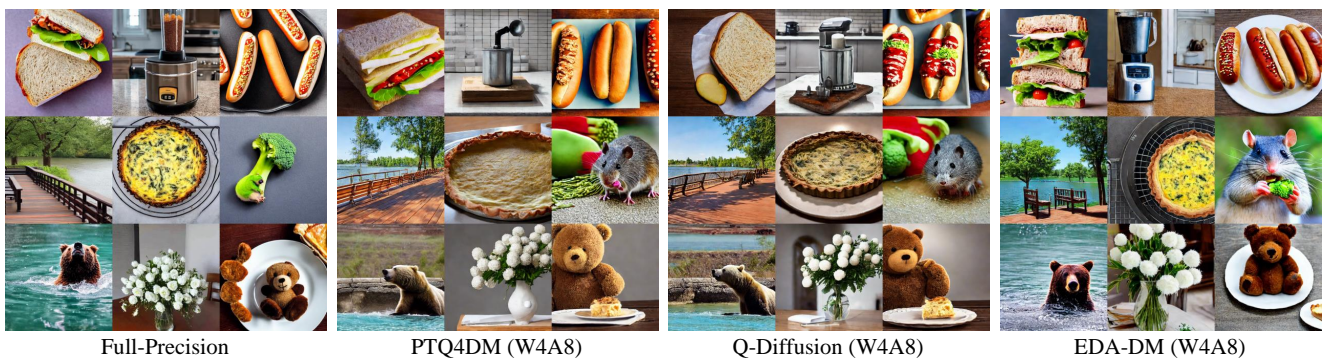
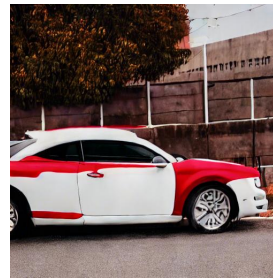
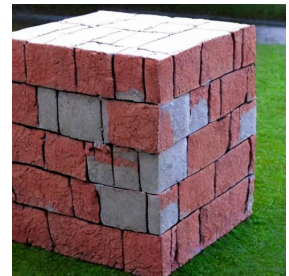
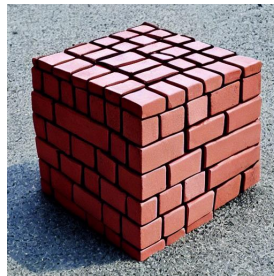


Figure 15: Random samples generated by Stable-Diffusion model on COCO dataset with W4A8 quantization.

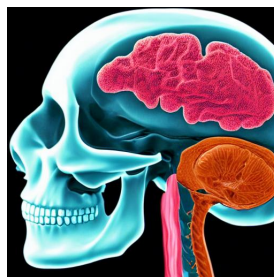
A white car and a red sheep.



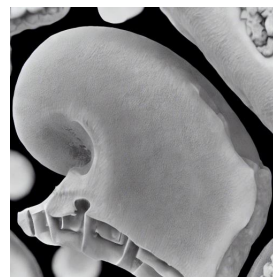
A cube made of brick.



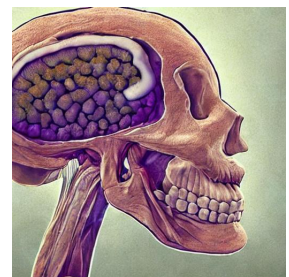
An organ of soft nervous tissue contained in the skull of vertebrates, functioning as the coordinating center of sensation and intellectual and nervous activity.



Full-precision (W32A32)



Q-Diffusion (W4A8)



EDA-DM (W4A8)

Figure 16: Human performance evaluation for Stable-Diffusion.